

Multiway Non-rigid Point Cloud Registration via Learned Functional Map Synchronization

Jiahui Huang, Tolga Birdal, Zan Gojcic, Leonidas J. Guibas, and Shi-Min Hu

Abstract—We present SyNoRiM, a novel way to jointly register multiple non-rigid shapes by synchronizing the maps relating learned functions defined on the point clouds. Even though the ability to process non-rigid shapes is critical in various applications ranging from computer animation to 3D digitization, the literature still lacks a robust and flexible framework to match and align a collection of real, noisy scans observed under occlusions. Given a set of such point clouds, our method first computes the pairwise correspondences parameterized via functional maps. We simultaneously learn potentially non-orthogonal basis functions to effectively regularize the deformations, while handling the occlusions in an elegant way. To maximally benefit from the multi-way information provided by the inferred pairwise deformation fields, we synchronize the pairwise functional maps into a *cycle-consistent* whole thanks to our novel and principled optimization formulation. We demonstrate via extensive experiments that our method achieves a state-of-the-art performance in registration accuracy, while being flexible and efficient as we handle both non-rigid and multi-body cases in a unified framework and avoid the costly optimization over point-wise permutations by the use of basis function maps. Our code is available at <https://github.com/huangjh-pub/synorim>.

Index Terms—3D Point Cloud, Non-rigid Registration, Functional Map Synchronization.

1 INTRODUCTION

THE prevalence of reliable 3D data capture fueled countless applications impacting from movie industry to robotics. In a wide variety of these applications, one needs to capture (in 3D) non-rigidly moving objects from multiple angles or over time [1], [2]. This leads to a dynamic, multi-scan alignment problem, further obstructed by the presence of occlusions, ambiguities, and noise.

Solving this challenging task fostered the development of a plethora of temporal, mesh-based dynamic non-rigid registration algorithms (e.g. [3]). However, these methods suffer from two main limitations: (1) the data provided by 3D sensors hardly come in mesh format, let alone the difficulty associated with preserving the mesh topology. Signed distance field based reconstruction methods like [4] can overcome some of these problems, but (2) they still assume a *streaming* depth map and fail to maintain correspondences, which are critical for defining non-rigid deformations. In addition to those nuisances, a drift-free alignment almost surely demands a global optimization step, which exploits all possible loop closure constraints in the form of a graph optimization [5] or bundle adjustment [6].

In this paper, we set off in pursuit of alleviating both of these issues. In particular, we (1) leverage unstructured point cloud representations for maximal generality and flexibility; (2) assume a fully connected graph in lieu of the sequential order, incorporating drift reduction in the early stages. Additionally, we make no assumptions on the object dynamics such as rigid motion [7], [8] or as rigid as possible deformations [9]. In particular, we propose SyN-

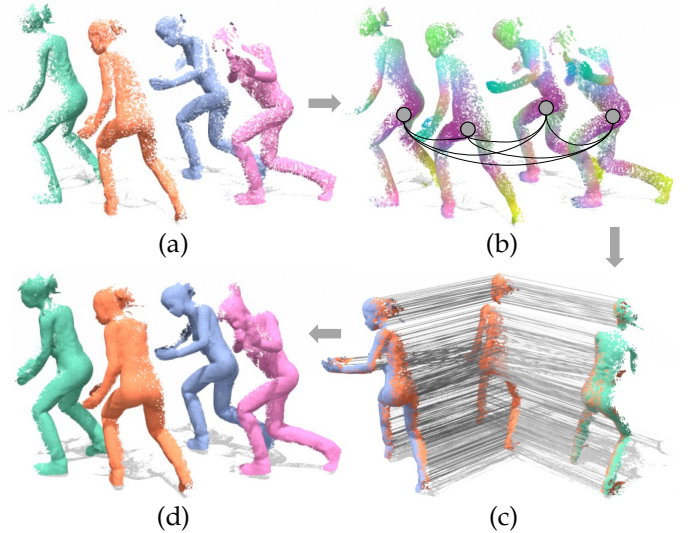


Fig. 1. **SyNoRiM overview.** (a) Input point clouds. (b) Synchronized canonical functions \mathbf{H} (dimension reduced by Principal Component Analysis (PCA); see § 5 for details). (c) Scene flow estimations for all pairs. (d) Registered (accumulated) point clouds by gathering warped points from other inputs.

oRiM framework, synchronization for non-rigid multiway registration. Input to SyNoRiM, is a collection of point cloud scans containing a potentially non-rigidly deforming object. We then seek to recover a coherent and consistent 3D scene flow, originating from any source shape to a latent target shape that is to be discovered simultaneously. We start by a *motion coherence observation* [10] that pairwise correspondences between natural shapes are smooth and band-limited, i.e. nearby points in the source point cloud should map to nearby points in the target (except for topological changes and occlusions). This allows us to substitute the point-wise matches between pairs of scans

- J. Huang and S.M. Hu are with the BNRist, Department of Computer Science and Technology, Tsinghua University.
Shi-Min Hu is the corresponding author.
- T. Birdal and L. J. Guibas are with Stanford University.
- Z. Gojcic is with Nvidia.

by linear maps of *learned smooth functions* defined on the points. Such notion of a *functional map* was first introduced in the geometry processing community [11] for estimating correspondences between isometric meshes. Unfortunately, due to the lack of proper basis functions, an extension to point cloud analysis is not trivial [12]. In SyNoRiM we propose to directly learn the bases from a large-scale training corpus, either in a fully-supervised or unsupervised fashion. Such bases learned by neural networks are found to be robust to occlusions, partiality, and errors in the initialization because an end-to-end training informs the bases about the shape context while the inherent smoothness enables meaningful extrapolations of the target coordinate functions. A subsequent *functional map synchronization* algorithm coerces the maps to be globally consistent, by making use of the information that individual observations are essentially samples from a common underlying surface. Based on this, we finally refine the pairwise deformations eliminating the ambiguities. An illustrative figure is shown in Fig. 1.

In summary, our contributions are:

- 1) We propose, to the best of our knowledge, the first end-to-end data-driven framework to learn consistent registration between multiple, possibly partial point cloud observations of non-rigidly moving bodies / objects.
- 2) Our deep network can learn potentially non-orthogonal functional bases on point sets without requiring to define Laplace-Beltrami operators (LBO). Functional maps between such bases can match non-isometric shapes.
- 3) We propose a novel *functional map synchronization* algorithm enforcing cycle-consistency among the pairwise deformation fields, estimated in isolation. This harmonizes the 3D flows into a coherent whole and thus enables multiway registration.

We demonstrate the efficacy of our algorithm through extensive evaluations on both rigid and non-rigid scenarios, showing superior performance on all datasets.

2 RELATED WORKS

Point-set Registration. Finding reliable alignments between point clouds plays a fundamental role for many downstream tasks. Rigid registration estimates a single transformation matrix through either heuristic searches [13] or learned local/global descriptors [14], [15], while common non-rigid registration techniques aim to best align the clouds under the various data terms [16], [17], [18] and regularizations [4], [9] with different deformation representations [19], [20]. In this paper we consider the general non-rigid deformation scheme and also demonstrate results on hybrid ones such as multibody [21]. On the other hand, scene flow describes the transition between two point clouds using a three-dimensional vector field and is a low-level task agnostic of the deformation type. Existing techniques [22], [23], [24], [25] handle the task via accurate modeling of the point-wise features as well as its neighborhood context, and reach a good performance for cluttered scenes or driving scenarios, but is not robust under large deformations and ambiguities [26].

Function-based Correspondence. In the field of geometry processing, the use of functional techniques is a recent trend for building reliable correspondences between 3D

shapes (e.g., discretized manifold meshes). First introduced in [11], such methods compute the LBO eigenvectors as basis functions and infer a linear transformation of a subset of bases to indicate low-rank shape mapping. Many extensions have been vastly explored such as hierarchical matching [27], partial-to-full handling [28] or integration into deep learning frameworks [29], [30] with either supervised or unsupervised [31], [32], [33] methods. Contrarily in the domain of point set analysis, such methods are less popular despite a few [34], [35], [36]. Notably, [35] also proposes to learn a linearly-invariant embedding as bases, yet their learning scheme is completely different from ours and they are not robust to partialities or occlusions which are commonly observed in point cloud data. We further highlight that the idea to project natural signals to lower dimensions has also been partially explored in the vision community [37], [38].

Synchronization on 3D Geometry. Though initially established as a theory for clock systems, synchronization has now been widely used in many vision tasks such as structure from motion [39], [40], semantic segmentation [41], permutation synchronization [42], [43] and multiway rigid/multibody registration [7], [44], [45]. By enforcing cycle consistencies within a system, the relative measurements are globally harmonized thanks to the averaging of local noise. In the field of 3D geometry analysis, analyzing and synchronizing spectral functional maps [46] from a mesh collection are widely applied to full shape matching, either with low-rank factorization [47], limit shapes extraction [48], coarse-to-fine strategy [49] or joint point-spectrum optimization [50]. In contrast, our novel synchronization formulation is tailored for the bases learned from raw point clouds that are free of the geometric impositions like (near-)isometries and directly takes correspondences into account, robustly.

3 OVERVIEW

Problem Formulation. The input to our method is a point cloud graph $\mathcal{G} := (\mathcal{V}, \mathcal{E})$, whose vertices \mathcal{V} represent the input set of K point clouds $\mathcal{V} := \{\mathbf{X}_k \in \mathbb{R}^{N_k \times 3}, k \in [1, K]\}$ and the edges $\mathcal{E} := \{(k, l), \mathbf{X}_k \in \mathcal{V}, \mathbf{X}_l \in \mathcal{V}\}$ represent the graph connectivity. By default we assume \mathcal{G} to be fully-connected. The output of our method contains all the pairwise per-point 3D flow vectors $\mathcal{F} := \{\mathbf{F}_{kl} \in \mathbb{R}^{N_k \times 3}, (k, l) \in \mathcal{E}\}$. The flow vectors naturally induce the non-rigid warp field from \mathbf{X}_k to \mathbf{X}_l as $\mathcal{W}_{kl}(\mathbf{X}_k) := \mathbf{X}_k + \mathbf{F}_{kl}$, optimally aligning the given point cloud pairs by deforming the source onto the target. We additionally encourage the cyclic consistency of the estimates \mathcal{F} , defined loosely as:

$$\mathcal{W}_{k_1 k_2} \circ \dots \circ \mathcal{W}_{k_{p-1} k_p} \circ \mathcal{W}_{k_p k_1} = \mathbf{I}, \forall (k_1, \dots, k_p) \in \mathcal{C}(\mathcal{G}), \quad (1)$$

where $\mathcal{C}(\mathcal{G})$ are the set of cycles in the \mathcal{G} and \mathbf{I} is the identity warping. The domain of the above composed warp map is the union region $(\mathbf{X}_{k_1}, \dots, \mathbf{X}_{k_p})$.

Method Summary. Our method begins by applying a basis network φ_{basis} independently to each input point cloud in order to generate a set of basis functions defined on the points (§ 4.2). Additionally, sparse point-level putative correspondences are established using a correspondence generator $\mathbf{g}(\cdot)$ (§ 4.3). Given the bases and sparse correspondences we can compute the initial pairwise functional map matrices. The technique to recover flows from the matrices

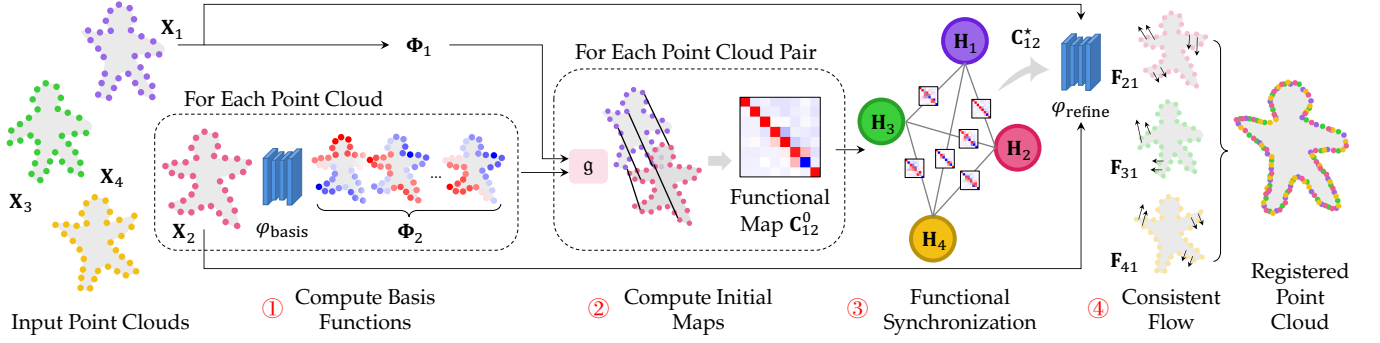


Fig. 2. **Pipeline.** Our methods starts with ① the estimation of basis functions with a network φ_{basis} ; then ② the initial functional maps $\{C_{kl}^0\}$ between all pairs of input points are built based on putative correspondences \mathbf{g} . ③ The maps are subsequently synchronized to optimize cycle consistency among the inputs. ④ 3D flow vectors are estimated from the optimized functional maps $\{C_{kl}^*\}$ as our final output.

is realized through another network φ_{refine} (§ 4.4). We then feed the initial map estimates into a synchronization module that jointly optimizes for all pairwise functional mappings, considering the cycle consistency (§ 5), before utilizing the φ_{refine} module once more to get the optimized deformations. The full pipeline is illustrated in Fig. 2.

4 PAIRWISE FUNCTIONAL REGISTRATION

4.1 Preliminaries on Functional Maps

Given two (abstract) shapes S_k and S_l in the form of smooth continuous manifolds, a functional map $T_{kl} : L_2(S_k) \mapsto L_2(S_l)$ maps from the space of square-integrable real-valued functions (L_2 -space) defined on S_k to S_l . Such an operator is proved to be linear [11], i.e., $T_{kl}(\alpha_1 f_1 + \alpha_2 f_2) = \alpha_1 T_{kl}(f_1) + \alpha_2 T_{kl}(f_2)$, where f_1 and f_2 are functions defined on S_k and α_1 and α_2 are the coefficients.

Every function f_k on S_k (or f_l on S_l) can be represented as a linear combination of *basis functions* $\{\phi_{k,m}\}$ (or $\{\phi_{l,m}\}$): $f_k = \sum_m h_{k,m} \phi_{k,m}$, $f_l = \sum_m h_{l,m} \phi_{l,m}$, with $h_{k,m}$ and $h_{l,m}$ being the coefficients. Moreover, most natural functions defined on shapes can be approximated by linearly combining a *finite* set of M bases, if correctly chosen. A functional map matrix $C_{kl} \in \mathbb{R}^{M \times M}$ can be then defined in replacement with T_{kl} , and satisfies $T_{kl}(\phi_{k,m_k}) = \sum_{m_l=1}^M (C_{kl})_{m_k, m_l} T_{kl}(\phi_{l,m_l})$, where $(C_{kl})_{m_k, m_l}$ denotes the element at the m_k -th row and the m_l -th column. We can then re-write the relation $f_l = T_{kl}(f_k)$ in linear algebra as $\mathbf{h}_k = C_{kl} \mathbf{h}_l$, where $\mathbf{h}_k := [h_{k,1}, \dots, h_{k,M}]^\top$, $\mathbf{h}_l := [h_{l,1}, \dots, h_{l,M}]^\top$. This reformulation admits various computation tools available for optimization. We refer readers to a full tutorial provided in [51] for more in-depth discussions.

Discretization on Point Clouds. As points are samples from the surfaces, we can define real-valued functions on each point cloud (e.g., \mathbf{X}_k) as a column vector in \mathbb{R}^{N_k} . Horizontally stacking the set of M basis functions $\{\phi_{k,m}\}_{m=1}^M$ gives a full-rank compact basis matrix $\Phi_k \in \mathbb{R}^{N_k \times M}$. The pairwise linear functional map matrix C_{kl} , when right-multiplied to Φ_k , linearly re-combines the bases from \mathbf{X}_k and yields the transferred set of bases Φ_l from \mathbf{X}_l to \mathbf{X}_k , i.e., $\Phi_k C_{kl} \approx \Pi_{kl} \Phi_l$, where Π_{kl} is the point-wise permutation matrix between the two point clouds. For other arbitrary functions $\mathbf{h} \in \mathbb{R}^{N_k}$, its coordinates under the bases are given by $\Phi_k^+ \mathbf{h}$, where \cdot^+ is the Moore-Penrose pseudo-inverse operator.

4.2 Computing Basis Functions

The basis functions play a critical role on the power of learned representations. For triangulated shapes where connectivity information is provided, bases can be easily formed via the standard method of decomposing the graph Laplacian [46]. Similarly, for point clouds one can also build a mesh structure such as a k-NN graph or intrinsic Delaunay triangulation [52] before computing the bases. However, the latter can be problematic because the constructed graph would have no notion of semantics or geodesics, leading to redundant or erroneous function approximation. Instead, we propose to learn the basis functions directly from point clouds using a sparse-convolution-based [53] neural network $\varphi_{\text{basis}} : \mathbf{X}_k \rightarrow \Phi_k$. Basis functions learned in such manner are both (1) accurate, i.e. focus only on the flow properties we are interested in, and (2) compact with no redundancies, as will be demonstrated in § 6, which allows achieving higher accuracy even with a small number of bases.

In order to train φ_{basis} , we compute the optimal functional maps as

$$C_{kl}^0 := \arg \min_{\mathbf{C}} E_{kl}(\mathbf{C}), \quad (2)$$

where

$$E_{kl}(\mathbf{C}) := \sum_{i=1}^{I_{kl}} \rho \left(\|\Phi_{l,i}^{(kl)} - \Phi_{k,i}^{(kl)} \mathbf{C}\| \right), \quad (3)$$

$$(\Phi_k^{(kl)}, \Phi_l^{(kl)}) = \mathbf{g}((\mathbf{X}_k, \Phi_k), (\mathbf{X}_l, \Phi_l)).$$

Here, $\mathbf{g}(\cdot)$ is a putative correspondence generator that will be detailed in § 4.3. It takes two point clouds as input, computes sparse correspondences, and selects the matched rows from Φ_k and Φ_l , producing $\Phi_k^{(kl)} \in \mathbb{R}^{I_{kl} \times M}$ and $\Phi_l^{(kl)} \in \mathbb{R}^{I_{kl} \times M}$, whose rows (the number of matches being I_{kl}) are indexed via $(\cdot)_{i:}$. During training we use the strategy similar to [54] by randomly instantiating \mathbf{g} either with the ground-truth \mathbf{g}_{gt} (if provided) or the predicted one \mathbf{g}_{pd} with a probability of 50%. We empirically observe the positive impact of this on final performance. $\rho(\cdot)$ is the Huber robust function [55] used for outlier rejection that individually treats each summand i . The scale of $\rho(\cdot)$ is chosen to be 0.05 and empirically we do not observe any significant difference using more advanced adaptive scales such as the median absolute deviations [56]. After obtaining C_{kl}^0 we feed it into the method in § 4.4 to compute the flow vectors, and supervise the networks using the loss function defined later in § 4.5.

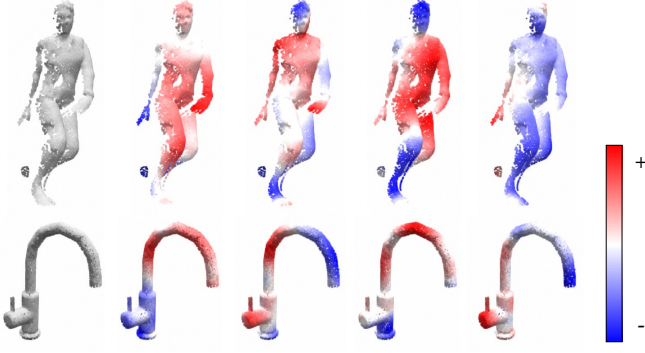


Fig. 3. **Learned bases visualization.** We visualize for two shapes (left) a chosen subset of its M bases. The basis range is normalized.

4.3 Generating Putative Correspondences

We estimate deep features $\mathbf{D}_k \in \mathbb{R}^{N_k \times F}$ for each point cloud in \mathcal{V} using a feature descriptor network $\varphi_{\text{desc}} : \mathbf{X}_k \rightarrow \mathbf{D}_k$. Given a pair of descriptors \mathbf{D}_k and \mathbf{D}_l , we construct the soft permutation matrix Π_{kl}^d and compute the scene flow as follows:

$$\begin{aligned} \mathbf{F}_{kl}^d &:= \Pi_{kl}^d \mathbf{X}_l - \mathbf{X}_k, \\ (\Pi_{kl}^d)_{ij} &:= \text{softmax}\left(\frac{1}{t^d} \|(\mathbf{D}_k)_i - (\mathbf{D}_l)_j\|\right), \end{aligned} \quad (4)$$

where t^d is a trainable parameter with the initial value of 1.0 and a minimum value of 0.02. $\text{softmax}(\cdot)$ performs softmax normalizations over all the rows of Π_{kl}^d so that it becomes row-stochastic. The flow loss \mathcal{L}_f introduced in § 4.5 will be used to supervise φ_{desc} until convergence.

After φ_{desc} is trained, it is fixed and we define the correspondence generator as $\mathbf{g}_{\text{pd}} : ((\mathbf{X}_k, \Phi_k), (\mathbf{X}_l, \Phi_l)) \rightarrow (\Phi_k^{(kl)}, \Phi_l^{(kl)})$, which selects *corresponding* rows (i.e., matched points) of the input bases. The row (point) indices are determined by a nearest neighbor search performed on the descriptors \mathbf{D}_k and \mathbf{D}_l with cross-check, and the rows are matched if the L2 distance of the descriptors is smaller than a *conservative* threshold of 0.3. Remarkably, such a simple strategy, similar to [24], already produces the flow \mathbf{F}_{kl}^d . However, as demonstrated in § 6.6, such an estimation is corrupted with noise, occlusions, and inconsistencies hence performing a lot worse than our full pipeline.

4.4 Recovering Flows from Functional Maps

Given a computed functional map matrix \mathbf{C}_{kl} , which could either be \mathbf{C}_{kl}^0 or the optimized one \mathbf{C}_{kl}^* from § 5, one can again compute the soft permutation matrix Π_{kl} between the two clouds and extract the flow as:

$$\begin{aligned} \mathbf{F}_{kl}^n &:= \Pi_{kl} \mathbf{X}_l - \mathbf{X}_k, \\ (\Pi_{kl})_{ij} &:= \text{softmax}\left(\frac{1}{t} \|(\Phi_k \mathbf{C}_{kl})_i - (\Phi_l)_j\|\right). \end{aligned} \quad (5)$$

However, as pointed out before, Π_{kl} is row-stochastic and the warped position $\Pi_{kl} \mathbf{X}_l$ hence never extends beyond the *convex hull* of \mathbf{X}_l , which is detrimental for computing flows for occluded points. An alternative way to compute the flow is to treat the target positions \mathbf{X}_l *themselves* as three functions and map their coordinates via \mathbf{C}_{kl} , evaluated as:

$$\mathbf{F}_{kl}^f := \Phi_k \mathbf{C}_{kl} \Phi_l^+ \mathbf{X}_l - \mathbf{X}_k. \quad (6)$$

Note that the ground-truth mapping already implies $\Phi_k \mathbf{C}_{kl} \approx \Pi_{kl} \Phi_l$ as noted in § 4.1. However, the two

methods for computing flows are fundamentally different, conceptually: \mathbf{F}_{kl}^f elegantly handles the issue of occlusions because the mapping allows us to map unknown positions to valid ranges given the continuity of the bases, leading to a learned extrapolation scheme via band-limited regularization. Nevertheless, the truncated basis may over-regularize the positions in geometrically-complicated parts and limit the representation power of the flows. In contrast, \mathbf{F}_{kl}^n can perform well on those regions thanks to notion of point-wise correspondences.

Hence, we combine the best of the two worlds by an additional refinement network φ_{refine} which digests the concatenation of the two, along with \mathbf{X}_k , and outputs the residual:

$$\mathbf{F}_{kl} := \mathbf{F}_{kl}^n + \varphi_{\text{refine}}([\mathbf{X}_k, \mathbf{F}_{kl}^f, \mathbf{F}_{kl}^n]). \quad (7)$$

The refinement network φ_{refine} is instantiated with a sparse-convolution-based network, which works in a coarse-to-fine fashion by first aligning the general cloud structure with \mathbf{F}_{kl}^f and then fixing small-scale detailed errors by considering the information from \mathbf{F}_{kl}^n . The smoothness property of such networks also helps prune predicted outliers as already demonstrated by previous works (e.g. [24]). A comparison between the different flows is shown in Fig. 6.

4.5 Loss and Training

We train our network in two steps, where: (1) We train the correspondence generator \mathbf{g} described in § 4.3 using a *flow loss* \mathcal{L}_f only, and (2) we jointly train φ_{basis} and φ_{refine} (§§ 4.2 and 4.4) end-to-end adding the *consistency loss* \mathcal{L}_c , i.e.:

$$\mathcal{L}_f + \lambda_c \mathcal{L}_c. \quad (8)$$

Notably, the argmin operator in Eq (2) is differentiated by computing the solution with Iteratively Reweighted Least Squares (IRLS) and unrolling the re-weighting iterations. We provide the details of this algorithm in Appendix B.

Flow Loss \mathcal{L}_f . If ground-truth annotations $\mathbf{F}_{kl}^{\text{gt}}$ are provided, we can directly use:

$$\mathcal{L}_{f,\text{sup}} := \|\mathbf{F}_{kl} - \mathbf{F}_{kl}^{\text{gt}}\|_F^2, \quad (9)$$

where $\|\cdot\|_F$ denotes Frobenius norm. Otherwise, we use the self-supervised loss inspired from [23]:

$$\mathcal{L}_{f,\text{unsup}} := \sum_{\text{type} \in \{\text{chamfer}, \text{smooth}, \text{lap}\}} \lambda_{\text{type}} \mathcal{L}_{\text{type}}, \quad (10)$$

where for conciseness, the respective loss terms $\mathcal{L}_{\text{type}}$, the weights being λ_{type} , are defined in Appendix A. We evaluate both settings using either $\mathcal{L}_{f,\text{sup}}$ or $\mathcal{L}_{f,\text{unsup}}$ in our experiments (see § 6.1 for details). The more general \mathcal{L}_f refers to both for convenience.

Consistency Loss \mathcal{L}_c . We impose the pairwise consistency loss [32] as:

$$\mathcal{L}_c := \|\mathbf{C}_{kl}^0 \mathbf{C}_{lk}^0 - \mathbf{I}_M\|_F^2, \quad (11)$$

where \mathbf{I}_M is the identity matrix with size $M \times M$. This loss regularizes the compound mapping from functions on \mathbf{X}_k to functions on \mathbf{X}_l and its backward forms an identity, ensuring a local consistency of the learned bases. Additionally, we tried other regularization terms over the bases, such as Laplacian commutativity [11]¹ or descriptor preservation [57] but empirically no improvement is observed.

1. This means to project the Laplacian operator \mathbf{L} to the current bases via $\Phi^+ \mathbf{L} \Phi$.

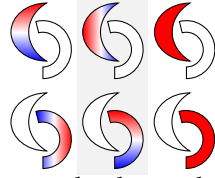
4.6 Discussions

Further Notice of Φ and \mathbf{C} . Examples of the learned basis functions are visualized in Fig. 3. Remarkably, the learned bases Φ and the functional map matrix \mathbf{C} are not constrained to a particular geometric structure, *e.g.*, orthonormality $\Phi^\top \Phi = \mathbf{I}$ or orthogonality $\mathbf{C}\mathbf{C}^\top = \mathbf{I}$, which hold only under isometric deformations with full geometry for meshes. The coarse-to-fine structure of Φ is not enforced either: the network finds its own way of representing high-frequency bases via learning small differences. Empirically we find that enforcing any of these regularizations harms the performance. On the other hand, unlike most existing works (*e.g.*, [29], [30]) that formulates Eq (3) by projecting *probe functions* $\mathbf{P}_k, \mathbf{P}_l$ via $\mathbf{C}_{kl}^0 := \arg \min_{\mathbf{C}} \|\mathbf{C}\Phi_l^\top \mathbf{P}_l - \Phi_k^\top \mathbf{P}_k\|$, our method is more robust due to the per-match outlier filtering and gets rid of the trade-off between the flexibility of probe functions and the compactness of the bases for flow estimation.

Special Case: Affinity Bases. For large-scale scenes with multiple moving *rigid* objects as often observed in the case of autonomous driving, the resulting flow can be effectively regularized by constraining the basis structure. Specifically, if the segmentation of S rigid bodies (each indexed by s) is known beforehand (*e.g.*, acquired via [8] or semantic segmentations), instead of learned ones, we can manually define the basis functions as:

$$\forall s, (\Phi_k)_{:,4s:4s+4} = \text{diag}(\mathbf{G}_k = s) [\mathbf{X}_k \quad \mathbf{1}], \quad (12)$$

where $\text{diag}(\cdot)$ is the diagonal matrix of an indicator vector, $\mathbf{G}_k \in \mathbb{R}^{N_k}$ are the rigid body indices corresponding to \mathbf{X}_k and the final bases $\Phi_k \in \mathbb{R}^{N_k \times 4S}$ are split into S blocks (as visualized in the inset as a 2D example). Note that the resulting map $\mathbf{C}_{kl} \in \mathbb{R}^{4S \times 4S}$ not only shows the affine transformation matrices in its 4×4 sub-blocks, but the sparsity of the sub-blocks also reveals rigid-body-level permutations. As a demonstration of the effectiveness of such bases, we provide evaluations on driving scenes in § 6.6.



5 FUNCTIONAL SYNCHRONIZATION

For a geometrically coherent outcome, we further ask the loops in \mathcal{G} to be closed. In our setting of functional mappings, this amounts to enforcing the cycle-consistency [43]:

$$\mathbf{C}_{k_1 k_2} \dots \mathbf{C}_{k_{p-1} k_p} \mathbf{C}_{k_p k_1} = \mathbf{I}, \quad \forall (k_1, \dots, k_p) \in \mathcal{C}(\mathcal{G}). \quad (13)$$

It can be easily shown by construction that the above formulation is equivalent to defining a set of V *canonical functions* $\mathbf{H}_k = [\mathbf{h}_k^1, \dots, \mathbf{h}_k^V] \in \mathbb{R}^{M \times V}$ on each point cloud \mathbf{X}_k , expressed as the coordinates under Φ_k . By enforcing the canonical functions to evaluate the same for the corresponding regions on different shapes, we define the following cycle consistency energy:

$$E_{\text{cycle}}(\{\mathbf{H}_k\}, \{\mathbf{C}_{kl}\}) := \sum_{(k,l) \in \mathcal{E}} \|\mathbf{H}_k - \mathbf{C}_{kl} \mathbf{H}_l\|_F^2. \quad (14)$$

Note that a naïve solution will collapse to $\mathbf{H}_k = \mathbf{0} \forall k$, so an additional orthonormality constraint is added as $\mathbf{H}^\top \mathbf{H} = \mathbf{I}_V$, where $\mathbf{H} := [\mathbf{H}_1^\top, \dots, \mathbf{H}_K^\top]^\top \in \mathbb{R}^{KM \times V}$. This constraint eliminates the trivial solution by *fixing the gauge* and encourages a larger functional space spanned by the canonical functions.

Additionally, we define the data term as the summation of all pairwise energies:

$$E_{\text{data}}(\{\mathbf{C}_{kl}\}) := \sum_{(k,l) \in \mathcal{E}} E_{kl}(\mathbf{C}_{kl}), \quad (15)$$

with E_{kl} defined in Eq (3). The solution to the problem

$$\arg \min_{\{\mathbf{H}_k\}, \{\mathbf{C}_{kl}\}} E_{\text{cycle}}(\{\mathbf{H}_k\}, \{\mathbf{C}_{kl}\}) + E_{\text{data}}(\{\mathbf{C}_{kl}\}) \quad (16)$$

gives us the synchronized functional maps $\{\mathbf{C}_{kl}^*\}$ as well as one possible set of canonical functions. After the optimization, we re-use the technique described in § 4.4 to recover \mathcal{F} as our final output, by feeding in the optimized result $\{\mathbf{C}_{kl}^*\}$ instead of $\{\mathbf{C}_{kl}^0\}$.

Analysis. In our formulation, each summand E_{kl} in E_{data} of Eq (15) now contains the robust function $\rho(\cdot)$ whose residual not only reflects the alignment with the current pairwise map, but also the consistency among all the maps in \mathcal{G} , related by $\{\mathbf{H}_k\}$. Remarkably, compared to existing point-based synchronization techniques (*e.g.* [7]), the use of functional maps is *lightweight* reducing the number of variables from the order of $O(N^2)$ to $O(M^2)$ where $M \ll N$. Besides, its additional degree-of-freedom endow us with more *flexibility* in representing non-rigid transformations compared to, *e.g.* [45].

Numerical Optimization. Inspired by [41], we use an alternating method to solve Eq (16). The optimization starts with the pairwise initialization $\{\mathbf{C}_{kl}^0\}$ obtained from Eq (2) and iterates over the following two steps:

- 1) **Optimizing $\{\mathbf{H}_k\}$ with fixed $\{\mathbf{C}_{kl}\}$.** As demonstrated in [7], after fixing $\{\mathbf{C}_{kl}\}$, the problem becomes a generalized Rayleigh problem with the orthonormality constraint, whose solution are the V eigenvectors of the graph connection Laplacian matrix \mathbf{L} corresponding to the V smallest eigenvalues. Please refer to Appendix C for detailed formulation of \mathbf{L} and the solution.
- 2) **Optimizing $\{\mathbf{C}_{kl}\}$ with fixed $\{\mathbf{H}_k\}$.** With $\{\mathbf{H}_k\}$ being considered as constant, the full problem is then decomposed into several small independent quadratic problems optimizing each \mathbf{C}_{kl} , $(k, l) \in \mathcal{E}$. Here, we once again use the IRLS technique for solving Eq (2) in a robust fashion: during each inner iteration the optimal solution $\mathbf{C}_{kl}^{[t]}$ (with t being the iteration count) is given by solving a closed-form $M^2 \times M^2$ linear system:

$$\begin{aligned} \text{vec}(\mathbf{C}_{kl}^{[t]}) &= \mathbf{\Gamma}_{kl}^{-1} \mathbf{b}_{kl}, \\ \mathbf{\Gamma}_{kl} &:= \mathbf{I} \otimes \mathbf{A}_{kl}^\top \mathbf{A}_{kl} + \mathbf{H}_l \mathbf{H}_l^\top \otimes \mathbf{I}, \\ \mathbf{b}_{kl} &:= \text{vec}(\mathbf{A}_{kl}^\top \mathbf{B}_{kl} + \mathbf{H}_k \mathbf{H}_l^\top), \end{aligned} \quad (17)$$

where \otimes is kronecker product, $\text{vec}(\cdot)$ is column-wise vectorization, $\mathbf{A}_{kl} := \mathbf{\Lambda}_{kl} \Phi_k^{(kl)}$, $\mathbf{B}_{kl} := \mathbf{\Lambda}_{kl} \Phi_l^{(kl)}$ and the computation of the diagonal weight matrix $\mathbf{\Lambda}_{kl} \in \mathbb{R}^{I_{kl} \times I_{kl}}$ is described in Appendix B.

The convergence criteria of the above optimization is defined as the mean relative change of each element in all pairwise \mathbf{C}_{kl} being less than 3×10^{-4} or exceeding the maximum number of iterations, which we set to 20.

Basis Preconditioning. While we do not regularize the columns of Φ_k to be orthogonal during the training of φ_{basis} , optimizations related to it can be highly ill-posed due to the emergence of near-parallel columns. This is due to the use of pseudo-inverse that implicitly factors out the high-frequency

bases from the network output, which by nature tends to produce over-smoothed results. Such a phenomenon, though does not affect network training without synchronization (*i.e.* § 4), jeopardizes the convergence and stability when jointly optimizing Eq (16). In order to mitigate this issue, during test time, we explicitly leverage orthogonality as a means of preconditioning by performing the singular value decomposition (SVD) as $\Phi_k = \mathbf{U}\Sigma\mathbf{V}^\top$ and replace Φ_k with \mathbf{U} as the new set of basis functions. Note that Eq (5) and Eq (6) are calibrated during training to engulf the original basis scale from the raw network output, hence the multiplier $\Sigma\mathbf{V}^\top$ should be applied back after synchronization to recover the final 3D flow vectors.

6 EXPERIMENTS

6.1 Dataset and Settings

Datasets. State-of-the-art methods for non-rigid registration or matching usually evaluate on different datasets with different settings. In order to provide a comprehensive and fair evaluation, we experiment with a full spectrum of possible input data, ranging from partial to full point clouds, from non-rigid human/clothes/animals to multi-body articulated objects, and from synthetic to real-world scenes. To this end, we extend the following datasets [58], [59], [60], [61], [62] to the task of multi-way non-rigid registration (hence the prefix **Multi-Point Cloud** used below):

- **MPC-CAPE** is sampled from CAPE [58], [59] dataset, which contains scanned sequences of clothed human using a commercial 3dMD scanner. We randomly sample non-consecutive K -frame snippets from the sequences and obtain the ground-truth flow from the fitted template mesh skinned via a Linear Blend Skinning [63] scheme.
- **MPC-DT4D** is from the DeformingThings4D [60] dataset, with hundreds of dynamic sequences of humanoids and animals whose skeletons and motions are designed by experts. We extract the partial point clouds by synthetically scanning the object under different motions.
- **MPC-DD** [61] contains partial views captured with a real RGB-D camera. The scene flows are provided by the original dataset via non-rigidly tracking the temporally densely-sampled frames.
- **MPC-SAPIEN** [62] consists of simulated, realistic, articulated object-level models that are commonly observed in daily life. We follow the data generation and sampling strategies implemented in [7].

Statistics of the dataset splits are shown in Tab. 1.

Metrics. The main metric for evaluating our flow quality is the (1) L2 Error, also termed as Mean Absolute Error (MAE), or End-Point Error (EPE), *i.e.*, the average norm of the flow error vectors over all points. We also include metrics from the scene flow [64] community but adapt their thresholds to our object-level setting. Specifically, we add: (2) 3D Accuracy Strict (AccS), the percentage of points whose relative error $< 5\%$ or $< 2\text{cm}$, (3) 3D Accuracy Relaxed (AccR), the percentage of points whose relative error $< 10\%$ or $< 5\text{cm}$, and (4) Outlier Ratio, the percentage of points whose relative error $> 30\%$.

In datasets with occlusions, we additionally compute all the metrics both for non-occluded points and the full point clouds. We subsequently collect the statistics among all the

TABLE 1

Dataset statistics. We report the number of training, validation and test samples used in the quantitative evaluations.

Dataset	# Train / Val.	# Test	Partial	Non-rigid	Real
MPC-CAPE [58], [59]	3015 / 798	209	-	✓	✓ [†]
MPC-DT4D [60]	3907 / 1707	1299	✓	✓	-
MPC-DD [61]	1754 / 200	267	✓	✓	✓
MPC-SAPIEN [62]	530 / 88	266	-	-	-

[†]: For train/val we use the points sampled from the parametric meshes while for test we use the raw-scanned point clouds.

$K(K-1)$ pairs of the metrics and report the mean value and standard deviation (\pm), the latter of which shows the consistency of the estimates among all individual pairs, as desired in the multiway setting.

Baselines. We compare the performance of SyNoRiM against a number of baselines grouped by the learning strategy. Hereinafter, we use the underlined names for brevity:

- **Non-learned:** Coherent Point Drift method (CPD) [17], Group-wise unnormalized information potential with Rényi’s entropy (GUIP) [65], and Non-Parametric Part (NPP) [66] using up to 25 RJ-MCMC sample steps;
- **Supervised:** Template-based methods 3D-CODED [67] and PTF [68] for MPC-CAPE only, Consistent ZoomOut (CZO) [49] where we replace the original Laplacian-Beltrami basis functions with the non-manifold one in [52] (the number of bases is set to 80), scene flow estimation methods including FLOT [24] and PointPWC-Net (PWC) [23], and MultiBodySync (MBS) [7] where for non-rigid case we remove the motion segmentation module and apply only the weighted permutation synchronization with downsampled 512 points;
- **Self-supervised:** PointPWC-Net (PWC-U) [23] with the unsupervised loss, and RMA-Net (RMA) [69] with the proposed differentiable rendering loss.

For baselines, which do not have a principled way of handling multiple inputs, we treat each pair of the input point clouds independently.

Parameter Settings. The networks φ_{desc} , φ_{basis} , and φ_{refine} are all trained using AdamW [70] optimizer with the initial learning rate of 10^{-3} and a 30% decay every 50k samples. φ_{desc} and φ_{basis} are both 4-layer U-Net with 32, 96, 64, 192 channels and 32, 64, 128, 256 channels respectively, while φ_{refine} is a 2-layer small network with 32 and 64 channels. All networks use InstanceNorm [71] as normalization. The initial t in Eq (5) is chosen to be 0.1, the weight for \mathcal{L}_c is $\lambda_c = 5 \times 10^{-3}$. For our self-supervised training scheme, we balance the Chamfer/Laplacian/smoothness losses with the weights 1.0/5.0/1.0, respectively. For benchmarking we choose $K = 4$ and use $M = 24$ for all of our experiments except for the one in § 6.6. V is set to be $M - 4$ for MPC-CAPE and $M - 2$ for all the other datasets.

6.2 Evaluations on MPC-CAPE

MPC-CAPE is mainly used to measure the fitting tightness and the deformation quality of the warped point clouds. As shown in Tab. 2, our method achieves a significant performance boost, reaching a 21.1% and 16.2% lower error compared to the nearest baseline under full supervision and self-supervised scenarios, respectively.

TABLE 2

Quantitative comparison on MPC-CAPE dataset using fully-supervised and self-supervised schemes. ↓ / ↑: Lower/higher is better (for the standard deviation being lower is always better). Supervision with 'Mesh' requires an additional template (or parametric) human mesh as a canonical prior. 'w/o sync.' is inferred from the initial functional map matrices without synchronization. **Boldfaced** numbers highlight the best and underlined numbers mark the tied first. Run time in (parentheses) denotes no GPU acceleration.

	Supervision	L2 Error ↓	AccS ↑	AccR ↑	Outlier ↓	Run Time (s)
CPD [17]	-	7.06 ± 2.46	2.5 ± 2.1	42.0 ± 20.3	90.8 ± 5.5	1.03
GUIP [65]	-	5.55 ± 2.16	35.8 ± 11.1	69.3 ± 13.4	80.9 ± 6.5	(28.2)
NPP [66]	-	19.02 ± 5.63	1.3 ± 1.7	10.6 ± 8.7	99.3 ± 0.9	(70.0)
CZO [49]	Full	2.04 ± 0.27	64.2 ± 7.5	94.2 ± 1.9	51.1 ± 10.7	(24.2)
3D-CODED [67]	Full + Mesh	2.25 ± 0.58	61.6 ± 9.0	95.4 ± 3.6	53.8 ± 11.2	160 [‡]
PTF [68]	Full + Mesh	2.52 ± 0.54	47.9 ± 12.8	91.4 ± 5.7	57.8 ± 9.6	100
PWC [23]	Full	1.37 ± 0.34	82.2 ± 8.4	98.3 ± 1.6	39.1 ± 10.4	0.99
FLOT [24]	Full	1.79 ± 0.34	69.9 ± 9.3	96.9 ± 2.0	48.4 ± 10.7	1.45
MBS [7]	Full	2.15 ± 0.22	54.0 ± 5.4	97.2 ± 1.8	55.9 ± 11.4	1.12
Ours	Full	1.08 ± 0.17	90.1 ± 4.3	99.5 ± 0.5	35.3 ± 10.1	1.22
PWC-U [23]	Self	3.52 ± 1.68	50.0 ± 13.6	82.7 ± 11.7	67.4 ± 8.7	0.99
RMA [69]	Self [†]	5.47 ± 2.29	$29.5 \pm \underline{15.0}$	67.9 ± 15.5	83.4 ± 7.0	1.60
Ours (w/o sync.)	Self	3.07 ± 1.37	53.9 ± 15.3	88.1 ± 8.7	$60.3 \pm \underline{11.0}$	0.32
Ours	Self	2.95 ± 1.29	$55.5 \pm \underline{15.0}$	89.1 ± 8.0	$59.1 \pm \underline{11.0}$	1.22

[†]: Fails to converge on our dataset if trained from scratch so we finetune from the pretrained model provided by the official repository.

[‡]: Includes the time for best rotation selection and test-time Chamfer loss minimization.

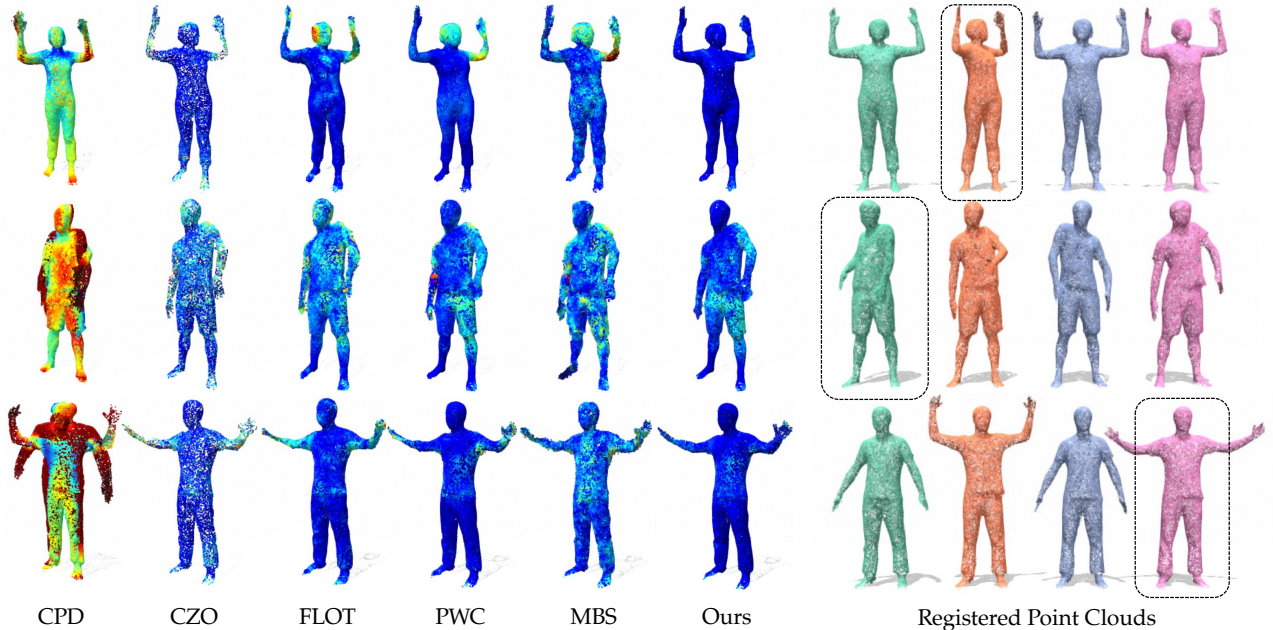



Fig. 4. **Comparison of fully-supervised MPC-CAPE.** Left: Color-coded per-point errors (0cm  10cm) are shown on the registered point clouds by warping all points to a selected pose. Right: Registered point clouds using our inferred 3D flows. Dashed rectangles are the views to which we warp other point clouds on the left side.

Referring to the visualizations in Fig. 4, SyNoRiM is most effective in point clouds with large changes, where traditional methods fail either due to wrong associations caused by matching ambiguity or insufficient degrees of warps. For learning-based methods: 3D-CODED and PTF rely on predefined canonical human shape prior, which prevents them from guaranteeing a tight fitting to the input points. CZO builds strict point-level correspondences. Hence, it is not capable of *densifying* the points and is error-prone once the number of outliers from φ_{basis} is large. Finally, while PWC and FLOT are trained using dense flow annotations and are free from large systematic errors, they still yield noisy estimates and result in shrunk artifacts in the detailed region. Comparably, we use the limited-band bases to effectively regularize the motions while preserving local rigidity and details. By explicitly projecting point-level matches onto

smooth functions, the generated warping is more accurate and robust to noise. In the unsupervised scenario, we are able to outperform PWC-U and RMA thanks to the superiority of our matching representation and the proposed learning strategy. Moreover, with the help of the synchronization module, we reach a better estimation by pruning inconsistent matches from the graph, reducing the standard deviation of the L2 error by over 5.8%.

6.3 Evaluations on MPC-DT4D

Scanned by a virtual camera, MPC-DT4D contains challenging partialities and occlusions, the handling which is an important yet often missing ingredient from many methods. Input shapes that overlap only partially can cause catastrophic failure for some methods that are incapable of

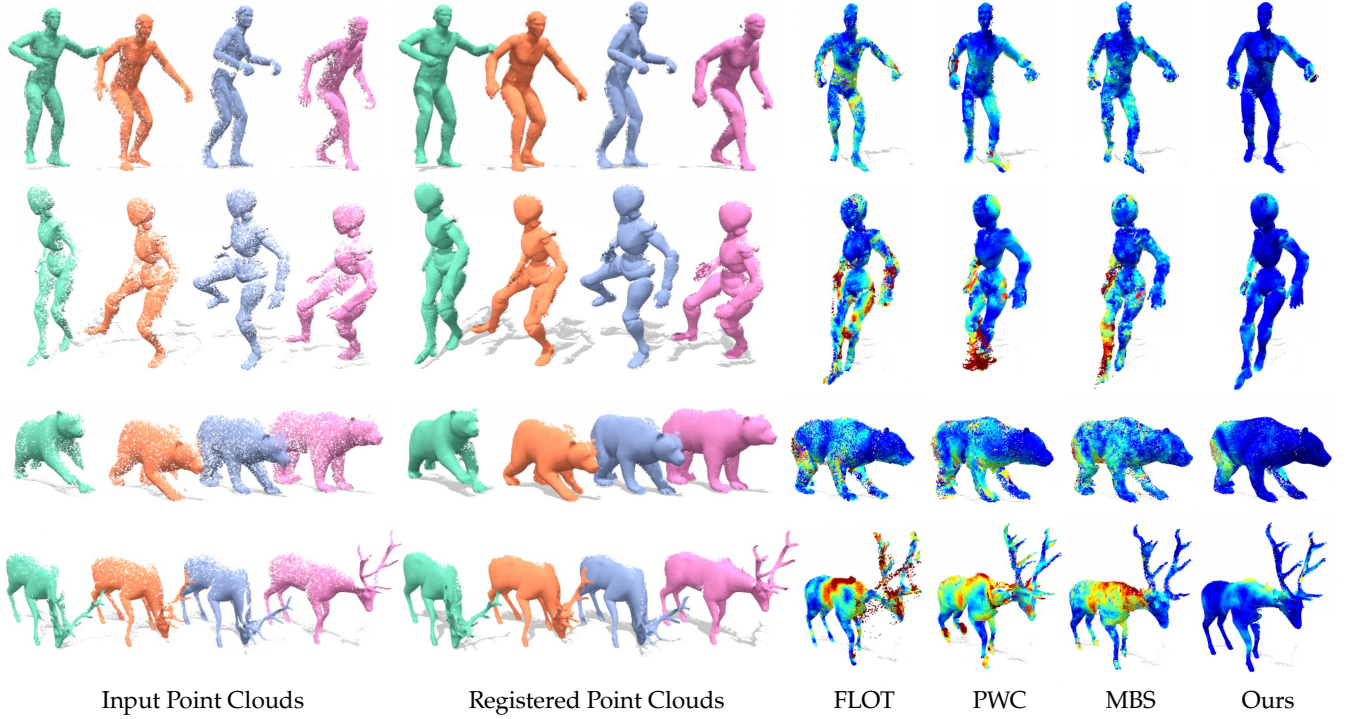


Fig. 5. **Comparison of different methods on the MPC-DT4D dataset.** The rightmost four columns show color-coded per-point errors (0cm 10cm) on the registered point clouds by warping all points to a selected pose.

TABLE 3

Quantitative comparison on MPC-DT4D dataset. We report results for both the non-occluded set of points and the full point cloud. See caption of Tab. 2 for other legends.

	Non-Occluded				Full			
	L2 Error ↓	AccS ↑	AccR ↑	Outlier ↓	L2 Error ↓	AccS ↑	AccR ↑	Outlier ↓
CPD [17]	10.12 ± 4.28	11.7 ± 8.9	43.2 ± 18.1	67.3 ± 12.8	10.91 ± 4.69	11.4 ± 8.6	41.8 ± 17.8	68.4 ± 12.3
GUIP [65]	16.43 ± 7.42	20.3 ± 8.9	43.0 ± 13.5	73.6 ± 10.6	17.22 ± 7.66	19.4 ± 8.8	41.2 ± 13.5	74.6 ± 10.2
CZO [49]	4.93 ± 1.62	42.4 ± 12.1	75.2 ± 10.3	37.8 ± 11.3	6.44 ± 2.45	39.8 ± 11.9	70.7 ± 11.2	40.8 ± 11.0
PWC [23]	5.39 ± 2.84	47.5 ± 14.0	77.0 ± 12.2	36.8 ± 12.5	6.35 ± 3.43	44.9 ± 13.9	73.2 ± 13.1	39.3 ± 12.5
FLOT [24]	5.14 ± 1.94	43.2 ± 11.7	75.3 ± 10.0	39.8 ± 10.9	6.57 ± 2.92	40.3 ± 11.6	70.5 ± 11.2	43.0 ± 10.9
MBS [7]	5.55 ± 2.45	43.9 ± 11.5	76.3 ± 11.1	38.4 ± 11.7	6.70 ± 3.13	41.2 ± 11.6	72.1 ± 12.1	41.1 ± 11.8
Ours (w/o sync.)	3.04 ± 1.54	<u>69.2</u> ± 10.7	89.5 ± 6.4	24.1 ± 10.1	3.73 ± 2.05	<u>65.5</u> ± 11.5	86.3 ± 8.0	26.0 ± 10.4
Ours	2.87 ± 1.25	<u>69.2</u> ± 10.2	89.8 ± 5.7	23.8 ± 9.7	3.53 ± 1.71	<u>65.5</u> ± 10.9	86.6 ± 7.2	25.6 ± 9.9

modeling the flow into *empty space*, especially when large deformations are present. Somewhat surprisingly, Tab. 3, shows that none of the SoTA methods can effectively deal with the hard problem setting presented in this dataset. On the one hand, methods like CZO and FLOT build the point-level correlation matrix (e.g. permutations), which results in large errors on the boundaries of the point cloud. On the other hand, the motion regularization implicitly introduced in CPD and GUIP cannot be easily adapted to the various kinds of input shapes. Moreover, the utilization of consistency on the level of points renders MBS inapplicable under such scenarios.

Comparably, as also shown in Fig. 5, we remark that in our method, the learning of the basis functions constructs a shared pattern of similar shapes under different views, hence producing a good functional extrapolation of point coordinates in a learned manner. By not operating on the level of points, our synchronization module bypasses the occlusion problem via aligning the globally-defined basis functions, successfully reducing the error by 5.4% for the full point cloud. Further challenging examples that can be successfully tackled by our method are visualized in Fig. 6.

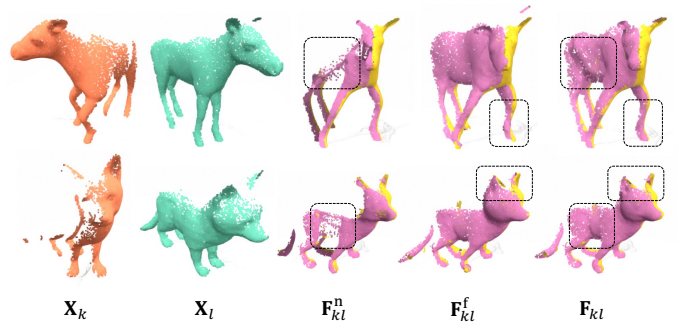


Fig. 6. **Handling low-overlap samples.** We warp two views () of the input to the third view () using different strategies for flow computation from the functional map matrix (See § 4.4 for notations and analysis). Dashed rectangles highlight the differences.

6.4 Evaluations on MPC-DD

As shown in Fig. 7, our method consistently outperforms scene-flow based methods (19.4% / 29.2% lower L2 Error and 2.9% / 11.3% higher AccS than FLOT / PWC, resp.), even with the presence of non-negligible real-world noise, holes, and large motions. We show the application of dynamic reconstruction from sparse views in Fig. 8 and found that

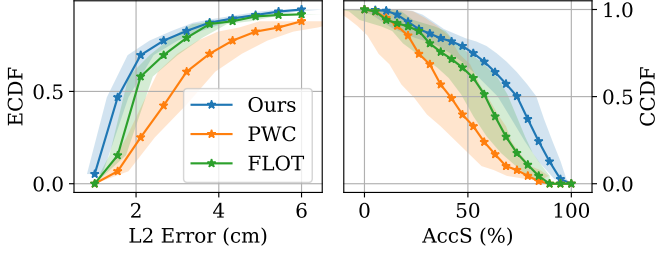


Fig. 7. **Quantitative comparison on MPC-DD dataset.** Left and right subfigures show the empirical cumulative distribution function (ECDF) and the complementary cumulative distribution function (CCDF) of L2 Error and AccS metrics. Higher curve is better. Shaded areas denote the standard deviations of the respective metrics among views.

our learned basis functions are smooth and robust, despite the difficulties in MPC-DD.

6.5 Evaluations on MPC-SAPIEN

Quantitative and qualitative evaluations on MPC-SAPIEN are shown in Tab. 4 and Fig. 9. Note, MPC-SAPIEN contains no occlusions and only small *local* deformations. This allows [52] to accurately estimate the point cloud bases, making CZO the most effective out of all the competitors. MBS is specially designed to handle multi-scan multi-body case, and already decreases the PWC backbone error by half thanks to the rigidity prior. However, the permutation and segmentation synchronization modules of MBS limit the maximum number of input points to hundreds coarsening the segmentation and causing a large overall error. As visualized earlier in Fig. 3, the basis functions learned from our method already contain motion cues whose patterns are similar to moving part segmentations. Hence, we conclude that our good performance stems mainly from the explicit usage of bases and the synchronization module, which itself contributes an 11.2% and 30.3% improvement over mean L2 Error and its variance, providing a better and more consistent flow estimation.

6.6 Affinity Bases on LidarKITTI

We now conduct an experiment on the cluttered scenes such as roads in autonomous driving to demonstrate the broad applicability of SyNoRiM. To this end, we use the LidarKITTI [8] dataset with ground points removed. Note that this dataset contains only pairwise Lidar frames, hence the synchronization module is not applied. The correspondence estimator \mathbf{g} is trained on FlyingThings3D [72] dataset with the hardest triplet loss as proposed in [73] and the bases are computed according to the *affinity bases* strategy in § 4.6 with the foreground segmentation module from [8].

The flow estimation results are listed in Tab. 5. Note that here the metric ratios use the original thresholds defined in [64]. Compared to our baselines, we reach a better performance, showing that the basis structure can effectively introduce meaningful priors to the scene flow estimation. Visualized in Fig. 10, the main error of our method comes from the affinely-warped background due to wrong raw correspondences estimated by \mathbf{g} . In fact, scene flow estimation in the wild achieves improved performance mainly due to more accurate ego-motion estimation as already pointed out in, e.g., [22] and our result can be further



Fig. 8. **Dynamic reconstruction on MPC-DD dataset** by accumulating the input point clouds. Left: RGB image of the reference frame (*ref*), which are *not* taken as input. Middle: Unprojected depth point cloud from *ref*. Right: Accumulated points by warping other 3 frames to *ref*.

TABLE 4
Quantitative comparison on MPC-SAPIEN dataset.
See caption of Tab. 2 for other legends.

	L2 Error ↓	AccS ↑	AccR ↑	Outlier ↓
CPD [17]	9.18 ± 4.50	7.4 ± 5.8	37.1 ± 22.7	81.3 ± 13.0
GUIP [65]	10.85 ± 4.28	10.0 ± 8.0	30.4 ± 16.8	84.7 ± 6.9
CZO [49]	3.40 ± 2.12	62.3 ± 14.5	86.9 ± 12.4	24.5 ± 11.8
PWC [23]	8.95 ± 3.86	7.3 ± 7.0	35.6 ± 20.9	81.3 ± 11.9
FLOT [24]	5.17 ± 2.69	32.9 ± 16.0	71.3 ± 18.6	45.6 ± 11.9
MBS [7]	4.93 ± 2.27	34.8 ± 14.4	72.8 ± 16.2	43.6 ± 10.5
Ours (w/o sync.)	3.48 ± 2.41	61.0 ± 19.0	86.2 ± 13.2	25.1 ± 11.9
Ours	3.09 ± 1.68	62.8 ± 15.3	88.1 ± 9.7	23.7 ± 9.6

TABLE 5
Comparisons on LidarKITTI Dataset. Rigid3DSceneFlow [8] exploits explicit rigid ego-motion estimation for the background scene flow. (φ_{basis} only) simply maps each point to its nearest neighbour in the feature space embedded by φ_{basis} .

	EPE3D ↓	AccS ↑	AccR ↑	Outliers ↓
PointPWC-Net [23]	39.0	38.7	55.0	65.3
FLOT [24]	65.3	15.5	31.3	83.7
Ours (φ_{basis} only)	62.4	31.6	46.3	72.5
Ours	28.9	37.4	58.7	68.2
Rigid3DSceneFlow [8]	15.3	48.5	73.0	46.6

improved if such rigidity constraint is added. Though, this is out of our current scope, as our aim is to validate the effectiveness of our affinity bases.

6.7 Ablation Studies

A. Number of Basis. The number of basis functions M reflects the prior knowledge on the intrinsic motion variability of the input shape. Tab. 6 shows that as the number of bases increases, the flow estimation error first decreases, but after passing a certain point, rises significantly. This is because the noise in the descriptors mistakenly incorporated into the learned bases start to dominate the increased representation power brought by adding more bases. In the meantime, computing the pseudo-inverse of a wider Φ_k matrix demands stronger numerical stability hampering the convergence of the entire model. In practice, we found that selecting $M = 24$ strikes a good balance between accuracy and computation time of the synchronization, which grows exponentially as M increases.

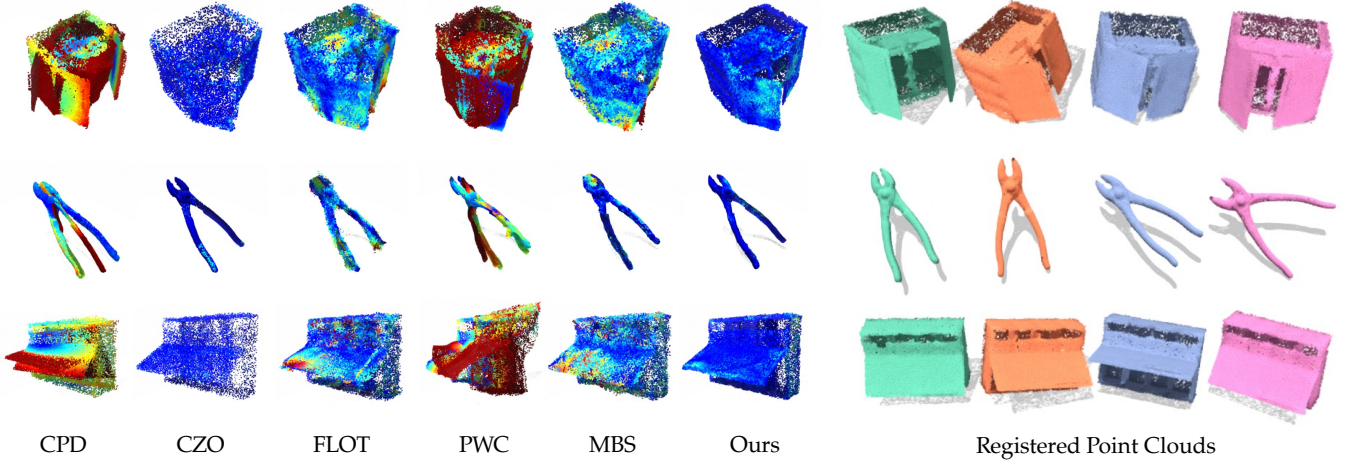


Fig. 9. **Comparison of fully-supervised MPC-SAPIEN.** Left: Color-coded per-point errors (0.0 to 0.1) are shown on the registered point clouds by warping all points to a selected pose. Right: Registered point clouds using our inferred scene flows for all input poses.

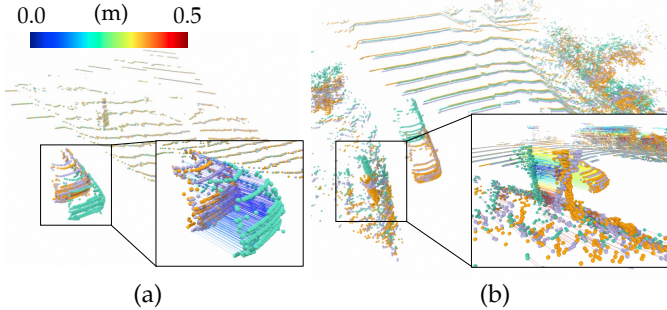


Fig. 10. **Results on LidarKITTI Dataset.** (a) and (b) show the best and worst result estimated using our method (L2 Errors are 2.1cm and 89.1cm). ■ Source points; ■ Target points; ■ Warped points.

TABLE 6
Performance using different number of bases on MPC-CAPE dataset. For run time we measure the average time for each iteration of our synchronization algorithm, in the unit of seconds.

# Basis M	L2 Error ↓	Run Time (sec./iter.)
8	1.14	6.0×10^{-3}
16	1.11	1.2×10^{-2}
24	1.08	2.6×10^{-2}
32	1.05	7.0×10^{-2}
64	1.27	1.9×10^0
80	1.55	5.9×10^0

B. Choice of Basis. Different basis functions defined on point clouds are available and we compare SyNoRiM to one of the non-learned methods [52]. Despite being proven by [74] to be *optimal* in representing smooth functions on manifold (in the sense that its gradient magnitudes are bounded), such bases functions are not task-tailored, whereas ours are learned to maximize the scene flow estimation performance and can work robustly under noise. As shown in Tab. 7, even with 80 bases, the flow recovered using [52] is worse than ours with only 24 bases. Moreover, the basis computation from a sparse convolution backbone accelerated with GPU is highly efficient and benefits from parallel implementation. The reduced number of bases not only makes the eigen-decomposition faster, but also boosts the efficiency of subsequent synchronization module.

TABLE 7
Comparison of our learned bases with [52] on MPC-CAPE dataset. Run time in (parentheses) denotes no GPU acceleration.

	# Basis	L2 Error ↓	AccS ↑	Run Time (sec.)	
				Basis	Sync. per iter.
[52]	24	2.96 ± 0.42	48.4 ± 8.2	(1.6)	0.03
	80	1.53 ± 0.21	78.4 ± 5.1	(3.2)	5.9
Ours	24	1.08 ± 0.17	90.1 ± 4.3	0.24	0.03

C. Training Scheme of φ_{basis} . We validate the effectiveness of the training strategies applied for φ_{basis} , including (a) the use of the robust term $\rho(\cdot)$, (b) the addition of the consistency loss \mathcal{L}_c and (c) the mixing strategy of \mathbf{g}_{gt} and \mathbf{g} . As demonstrated in Tab. 8, adding the robust term gives the framework more tolerance towards noise while the consistency loss acts as an efficient regularizer and speeds up network convergence. Apart from the performance gain from the mixing strategy, we empirically found that using only the ground-truth \mathbf{g} causes singularities in the network prediction which gives ill-posed scene flow when two frames are too close.

D. Refinement Strategy. We show that the combination of flows is indeed helpful, especially in the occluded regions. By definition, \mathbf{F}^n is not capable of transferring points to the empty region where \mathbf{F}^f comes to the rescue by extending the target mapped positions to the full 3D space (c.f. Fig. 6 for visual comparisons). As illustrated in Tab. 9, feeding the three pieces of information altogether helps the refinement module achieve the best result.

E. Effect of Synchronization. Synchronization links the information from multiple input point clouds exploiting cycle consistency and reduces the overall error. Here, we ablate different optimization strategies in Tab. 10 using MPC-SAPIEN dataset. The use of the robust term $\rho(\cdot)$, different from the one used for pairwise training, now jointly considers multi-scan cues and prunes the inconsistent outliers which is hard to detect in the pairwise setting. Although the basis preconditioning (Basis Precond.) strategy does not result in a large performance difference at convergence, it has a positive

TABLE 8

Comparisons of different φ_{basis} training strategies on MPC-DT4D dataset. See text for the explanation of (a),(b),(c). The values of EPE3D are measured on (non-occluded / full) point clouds.

(a) $\rho(\cdot)$	(b) \mathcal{L}_c	(c) Mixed g	L2 Error $\mathbf{F}^n \downarrow$	L2 Error $\mathbf{F}^f \downarrow$
			3.64 / 5.62	4.33 / 6.05
✓			3.58 / 5.48	4.13 / 5.78
✓	✓		3.52 / 5.41	4.16 / 5.78
✓		✓	3.49 / 5.38	4.11 / 5.74
✓	✓	✓	3.23 / 4.76	4.19 / 5.49
✓	✓	✓	3.14 / 4.59	3.86 / 5.09

TABLE 9

Comparisons of different refinement strategies on MPC-DT4D dataset to generate the final 3D scene flow. L2 Errors are measured on (non-occluded / full) point clouds. For the first line we use \mathbf{F}^n directly.

φ_{refine} with input \mathbf{F}^n	Input + \mathbf{F}^f	Input + \mathbf{X}	L2 Error \downarrow
			3.14 / 4.59
✓			3.09 / 3.91
✓	✓		3.04 / 3.81
✓		✓	3.04 / 3.73

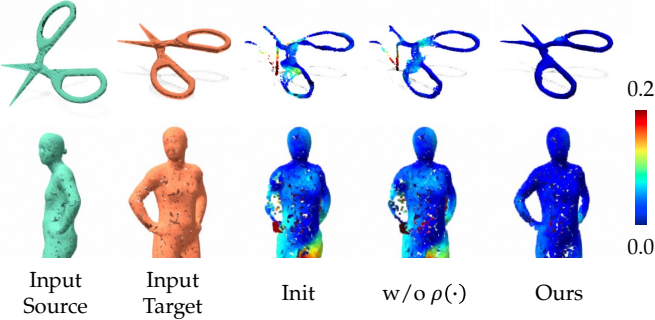


Fig. 11. **Visual comparison of the synchronization effect.** Flow error is shown on the warped source point cloud. The last 2 columns are computed using additional inputs (not shown here) for synchronization.

TABLE 10

Comparison of different synchronization methods on MPC-SAPIEN dataset. ‘Fixed Iter.’ denotes optimizing for a fixed number of iterations, while ‘Converged Iter.’ means to iterate until convergence. ‘Time’ measures the full run time of the synchronization module.

	Fixed Iter. L2 Error \downarrow	Converged Iter. L2 Error \downarrow	Time (s)	# Iter (k)
Init. (w/o sync.)	3.48 \pm 2.41	-	-	-
Spectral [7]	3.24 \pm 1.57	-	-	-
w/o $\rho(\cdot)$	3.31 \pm 1.90	3.18 \pm 1.79	4.2	0.2
w/o Basis Precond.	3.17 \pm 1.87	3.03 \pm 1.57	16.7	0.72
w/o Alter. Optim.	3.27 \pm 1.87	3.00 \pm 1.55	(45.5)	1.0
Ours Full	3.09 \pm 1.68	3.03 \pm 1.56	7.0	0.32

impact on the convergence rate. As a direct replacement to our alternating optimization scheme (Alter. Optim.), we borrow the solver from [75] to jointly optimize \mathbf{H} and \mathbf{C} on the product manifold of Stiefel and Euclidean. At convergence, this direct optimizer reaches a slightly lower error. Nevertheless, a lower flow error does not necessarily indicate a better convergence of Eq (16) and vice versa. We conclude, though, that our optimization scheme can reach a *decent performance* with *much better efficiency* than its counterparts. Please see Fig. 11 for visual comparisons.

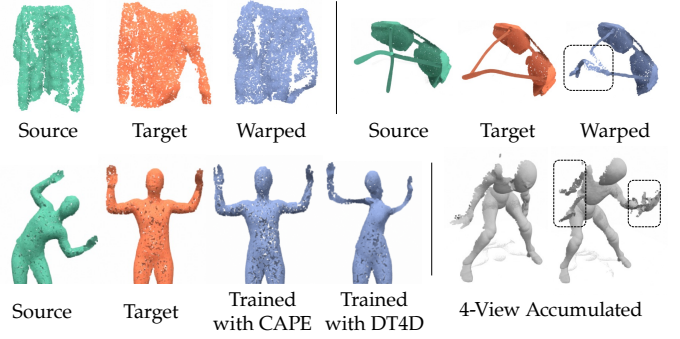
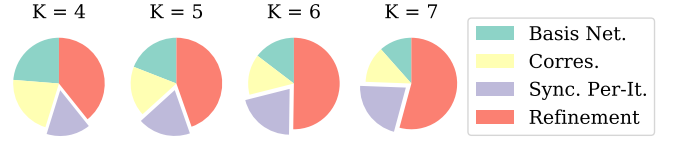


Fig. 12. **Failure Cases.** Typical failure cases of SyNoRiM includes large topological changes and matching ambiguities, along with limited generalizability to a different domain.

6.8 Timing and Memory Analysis



We evaluate the efficiency of SyNoRiM on a workstation with a 3.70GHz Intel i9 CPU with a single GeForce RTX 3090 graphics card. On average it takes 1.22s, 1.86s, 2.80s, 3.89s to generate 12, 20, 30, 42 pairs of flow vectors for $K = 4, 5, 6, 7$ (i.e., roughly 100ms/pair), respectively. The detailed breakdown of the relative time cost by each component is shown in the pie chart above: while the refinement module (■) takes more time than φ_{basis} (■) and computing \mathbf{g} (■) when K gets larger (because the number of pairs grow quadratically), the synchronization module (■) is always the one that dominates the computation. We find that the training of both φ_{basis} and φ_{refine} usually reaches a full converge within two days, while baselines like PWC take more than 5 days. The parameters for φ_{basis} , φ_{desc} and φ_{refine} are 8.8M, 5.0M and 0.7M, respectively. Runtime memory footprint for the entire pipeline is around 2.8GiB for $K = 4$.

7 CONCLUSION

In this paper we present SyNoRiM, a novel method for multiway non-rigid point cloud registration. In our framework, we learn the basis functions defined on the domain of point clouds and represent the registration under the framework of functional maps, endowing us with both efficiency and flexibility. The maps are then digested by our robust synchronization module to incorporate cycle-consistency constraints into the solution, producing more accurate scene flow estimates. Our method leverages ideas from computer graphics community concerned with processing clean geometry and applies these ideas to the task of computer vision where occlusions and noise are inevitable. The good performance of SyNoRiM on a full spectrum of cases gives hope for future works in bridging the gap between these two schools.

Limitations. Despite the state-of-the-art performance, SyNoRiM also has some limitations which we point out in the following and illustrate in Fig. 12: (1) the estimated bases sometimes overly-regularize the motion under large

displacements and topological changes, causing wrong parts to be stitched together; (2) SyNoRiM is less robust to handling motion ambiguities caused by severe occlusions — in the extreme case \mathbf{C} will be ill-conditioned if the corresponding functional coordinates amount to zero; and (3) we find that the trained network has difficulties to generalize to new domains (e.g. from humans to animals/objects). This is partially due to the global field-of-view we employed in our basis network being easily fitted to the entire object structure.

Future Work. Besides addressing aforementioned limitations, SyNoRiM leaves ample room for future works, including better representation of the deformation flow and incorporating more priors to capture complicated motions.

REFERENCES

- [1] M. Dou, H. Fuchs, and J.-M. Frahm, “Scanning and tracking dynamic objects with commodity depth cameras,” in *IEEE Int. Symposium Mixed and Augmented Reality*. IEEE, 2013, pp. 99–106. [1](#)
- [2] A. Collet, M. Chuang, P. Sweeney, D. Calabrese, H. Hoppe, A. G. Kirk, and S. Sullivan, “High-quality streamable free-viewpoint video,” *ACM TOG*, vol. 34, pp. 1–13, 2015. [1](#)
- [3] R. A. Newcombe, D. Fox, and S. M. Seitz, “Dynamicfusion: Reconstruction and tracking of non-rigid scenes in real-time,” in *Proc. IEEE Conf. CVPR*, 2015, pp. 343–352. [1](#)
- [4] M. Slavcheva, M. Baust, and S. Ilic, “Sobolevfusion: 3d reconstruction of scenes undergoing free non-rigid motion,” in *Proc. IEEE Conf. CVPR*, 2018, pp. 2646–2655. [1, 2](#)
- [5] T. Birdal, U. Şimşekli, M. O. Eken, and S. Ilic, “Bayesian pose graph optimization via bingham distributions and tempered geodesic mcmc,” in *NeurIPS*, 2018. [1](#)
- [6] B. Triggs, P. F. McLauchlan, R. I. Hartley, and A. W. Fitzgibbon, “Bundle adjustment—a modern synthesis,” in *International workshop on vision algorithms*. Springer, 1999, pp. 298–372. [1](#)
- [7] J. Huang, H. Wang, T. Birdal, M. Sung, F. Arrigoni, S.-M. Hu, and L. J. Guibas, “Multibodysync: Multi-body segmentation and motion estimation via 3d scan synchronization,” in *Proc. IEEE Conf. CVPR*, 2021, pp. 7108–7118. [1, 2, 5, 6, 7, 8, 9, 11, 14](#)
- [8] Z. Gojcic, O. Litany, A. Wieser, L. J. Guibas, and T. Birdal, “Weakly supervised learning of rigid 3d scene flow,” in *Proc. IEEE Conf. CVPR*, 2021, pp. 5692–5703. [1, 5, 9](#)
- [9] O. Sorkine and M. Alexa, “As-rigid-as-possible surface modeling,” in *Symposium on Geometry Processing*, vol. 4, 2007, pp. 109–116. [1, 2](#)
- [10] A. L. Yuille and N. M. Grzywacz, “The motion coherence theory,” in *Proc. IEEE Int. Conf. Computer Vision*, 1988. [1](#)
- [11] M. Ovsjanikov, M. Ben-Chen, J. Solomon, A. Butscher, and L. Guibas, “Functional maps: a flexible representation of maps between shapes,” *ACM TOG*, vol. 31, no. 4, pp. 1–11, 2012. [2, 3, 4](#)
- [12] R. Huang, F. Chazal, and M. Ovsjanikov, “On the stability of functional maps and shape difference operators,” in *Computer Graphics Forum*, vol. 37, no. 1, 2018, pp. 145–158. [2](#)
- [13] K. S. Arun, T. S. Huang, and S. D. Blostein, “Least-squares fitting of two 3-d point sets,” *IEEE Trans. on Pattern Analysis and Machine Intelligence*, vol. 9, no. 5, pp. 698–700, 1987. [2](#)
- [14] S. Ao, Q. Hu, B. Yang, A. Markham, and Y. Guo, “Spinnet: Learning a general surface descriptor for 3d point cloud registration,” in *Proc. IEEE Conf. CVPR*, 2021, pp. 11753–11762. [2](#)
- [15] S. Huang, Z. Gojcic, M. Usvyatsov, A. Wieser, and K. Schindler, “Predator: Registration of 3d point clouds with low overlap,” in *Proc. IEEE Conf. CVPR*, 2021, pp. 4267–4276. [2](#)
- [16] B. Amberg, S. Romdhani, and T. Vetter, “Optimal step nonrigid icp algorithms for surface registration,” in *Proc. IEEE Conf. CVPR*, 2007, pp. 1–8. [2](#)
- [17] A. Myronenko and X. Song, “Point set registration: Coherent point drift,” *IEEE Trans. on Pattern Analysis and Machine Intelligence*, vol. 32, no. 12, pp. 2262–2275, 2010. [2, 6, 7, 8, 9](#)
- [18] Y. Yao, B. Deng, W. Xu, and J. Zhang, “Quasi-newton solver for robust non-rigid registration,” in *Proc. IEEE Conf. CVPR*, 2020, pp. 7600–7609. [2](#)
- [19] R. W. Sumner, J. Schmid, and M. Pauly, “Embedded deformation for shape manipulation,” *ACM TOG*, vol. 26, no. 3, p. 80–es, 2007. [2](#)
- [20] A. Bozic, P. Palafox, M. Zollhofer, J. Thies, A. Dai, and M. Nießner, “Neural deformation graphs for globally-consistent non-rigid reconstruction,” in *Proc. IEEE Conf. CVPR*, 2021, pp. 1450–1459. [2](#)
- [21] J. P. Costeira and T. Kanade, “A multibody factorization method for independently moving objects,” *Int. Journal of Computer Vision*, vol. 29, no. 3, 1998. [2](#)
- [22] S. A. Baur, F. Moosmann, P. Pinggera, B. Ommer, and A. Geiger, “Slim: Self-supervised lidar scene flow and motion segmentation,” in *Proc. IEEE Int. Conf. Computer Vision*, 2021, pp. 13126–13136. [2, 9](#)
- [23] W. Wu, Z. Y. Wang, Z. Li, W. Liu, and L. Fuxin, “Pointpwc-net: Cost volume on point clouds for (self-) supervised scene flow estimation,” in *European Conference on Computer Vision*, 2020, pp. 88–107. [2, 4, 6, 7, 8, 9, 14](#)
- [24] G. Puy, A. Boulch, and R. Marlet, “FLOT: Scene Flow on Point Clouds Guided by Optimal Transport,” in *European Conference on Computer Vision*, 2020, pp. 527–544. [2, 4, 6, 7, 8, 9](#)
- [25] R. Li, G. Lin, T. He, F. Liu, and C. Shen, “Hcrf-flow: Scene flow from point clouds with continuous high-order crfs and position-aware flow embedding,” in *Proc. IEEE Conf. CVPR*, 2021, pp. 364–373. [2](#)
- [26] B. Ouyang and D. Raviv, “Occlusion guided self-supervised scene flow estimation on 3d point clouds,” *arXiv preprint arXiv:2104.04724*, 2021. [2](#)
- [27] S. Melzi, J. Ren, E. Rodolà, A. Sharma, P. Wonka, and M. Ovsjanikov, “Zoomout: Spectral upsampling for efficient shape correspondence,” *ACM TOG*, vol. 38, no. 6, 2019. [2](#)
- [28] O. Litany, E. Rodolà, A. M. Bronstein, and M. M. Bronstein, “Fully spectral partial shape matching,” in *Computer Graphics Forum*, vol. 36, no. 2, 2017, pp. 247–258. [2](#)
- [29] N. Donati, A. Sharma, and M. Ovsjanikov, “Deep geometric functional maps: Robust feature learning for shape correspondence,” in *Proc. IEEE Conf. CVPR*, 2020, pp. 8592–8601. [2, 5](#)
- [30] O. Litany, T. Remez, E. Rodolà, A. M. Bronstein, and M. M. Bronstein, “Deep functional maps: Structured prediction for dense shape correspondence,” in *Proc. IEEE Int. Conf. Computer Vision*, 2017, pp. 5659–5667. [2, 5](#)
- [31] M. Eisenberger, A. Tokor, L. Leal-Taixé, and D. Cremers, “Deep shells: Unsupervised shape correspondence with optimal transport,” in *NeurIPS*, 2020. [2](#)
- [32] J.-M. Roufousse, A. Sharma, and M. Ovsjanikov, “Unsupervised deep learning for structured shape matching,” in *Proc. IEEE Int. Conf. Computer Vision*, 2019, pp. 1617–1627. [2, 4](#)
- [33] O. Halimi, O. Litany, E. Rodolà, A. M. Bronstein, and R. Kimmel, “Unsupervised learning of dense shape correspondence,” in *Proc. IEEE Conf. CVPR*, 2019, pp. 4370–4379. [2](#)
- [34] R. Magnet and M. Ovsjanikov, “Dwks: A local descriptor of deformations between meshes and point clouds,” in *Proc. IEEE Int. Conf. Computer Vision*, 2021, pp. 3793–3802. [2](#)
- [35] R. Marin, M.-J. Rakotosaona, S. Melzi, and M. Ovsjanikov, “Correspondence learning via linearly-invariant embedding,” in *NeurIPS*, 2020. [2](#)
- [36] N. Sharp, S. Attai, K. Crane, and M. Ovsjanikov, “Diffusionnet: Discretization agnostic learning on surfaces,” *ACM TOG*, vol. 0, no. 0, 2021. [2](#)
- [37] C. Tang, L. Yuan, and P. Tan, “Lsm: Learning subspace minimization for low-level vision,” in *Proc. IEEE Conf. CVPR*, 2020. [2](#)
- [38] N. Ye, C. Wang, H. Fan, and S. Liu, “Motion basis learning for unsupervised deep homography estimation with subspace projection,” in *Proc. IEEE Int. Conf. Computer Vision*, 2021, pp. 13117–13125. [2](#)
- [39] R. Hartley, J. Trumpf, Y. Dai, and H. Li, “Rotation averaging,” *Int. Journal of Computer Vision*, vol. 103, no. 3, 2013. [2](#)
- [40] T. Birdal, M. Arbel, U. Simsekli, and L. J. Guibas, “Synchronizing probability measures on rotations via optimal transport,” in *Proceedings of the IEEE/CVF Conference on Computer Vision and Pattern Recognition*, 2020, pp. 1569–1579. [2](#)
- [41] F. Wang, Q. Huang, and L. J. Guibas, “Image co-segmentation via consistent functional maps,” in *Proc. IEEE Int. Conf. Computer Vision*, 2013, pp. 849–856. [2, 5](#)
- [42] T. Birdal and U. Simsekli, “Probabilistic permutation synchronization using the riemannian structure of the birkhoff polytope,” in *Proc. IEEE Conf. CVPR*, 2019, pp. 11105–11116. [2](#)
- [43] T. Birdal, V. Golyanik, C. Theobalt, and L. J. Guibas, “Quantum permutation synchronization,” in *Proceedings of the IEEE/CVF Conference on Computer Vision and Pattern Recognition*, 2021, pp. 13122–13133. [2, 5](#)
- [44] X. Huang, Z. Liang, and Q. Huang, “Uncertainty quantification for multi-scan registration,” *ACM TOG*, vol. 39, no. 4, 2020. [2](#)

- [45] Z. Gojcic, C. Zhou, J. D. Wegner, L. J. Guibas, and T. Birdal, "Learning multiview 3d point cloud registration," in *Proc. IEEE Conf. CVPR*, 2020, pp. 1759–1769. [2, 5](#)
- [46] H. Zhang, O. Van Kaick, and R. Dyer, "Spectral mesh processing," in *Computer Graphics Forum*, vol. 29, no. 6, 2010, pp. 1865–1894. [2, 3](#)
- [47] Q. Huang, F. Wang, and L. Guibas, "Functional map networks for analyzing and exploring large shape collections," *ACM TOG*, vol. 33, no. 4, pp. 1–11, 2014. [2](#)
- [48] R. Huang, P. Achlioptas, L. Guibas, and M. Ovsjanikov, "Limit shapes—a tool for understanding shape differences and variability in 3d model collections," in *Computer Graphics Forum*, vol. 38, no. 5, 2019, pp. 187–202. [2](#)
- [49] R. Huang, J. Ren, P. Wonka, and M. Ovsjanikov, "Consistent zoomout: Efficient spectral map synchronization," in *Computer Graphics Forum*, vol. 39, no. 5, 2020, pp. 265–278. [2, 6, 7, 8, 9](#)
- [50] M. Gao, Z. Lahner, J. Thunberg, D. Cremers, and F. Bernard, "Isometric multi-shape matching," in *Proc. IEEE Conf. CVPR*, 2021, pp. 14183–14193. [2](#)
- [51] M. Ovsjanikov, E. Corman, M. Bronstein, E. Rodolà, M. Ben-Chen, L. Guibas, F. Chazal, and A. Bronstein, "Computing and processing correspondences with functional maps," in *SIGGRAPH ASIA 2016 Courses*, 2016, pp. 1–60. [3](#)
- [52] N. Sharp and K. Crane, "A laplacian for nonmanifold triangle meshes," in *Computer Graphics Forum*, vol. 39, no. 5, 2020, pp. 69–80. [3, 6, 9, 10](#)
- [53] C. Choy, J. Gwak, and S. Savarese, "4d spatio-temporal convnets: Minkowski convolutional neural networks," in *Proc. IEEE Conf. CVPR*, 2019, pp. 3075–3084. [3](#)
- [54] S. Bengio, O. Vinyals, N. Jaitly, and N. Shazeer, "Scheduled sampling for sequence prediction with recurrent neural networks," in *NeurIPS*, 2015, p. 1171–1179. [3](#)
- [55] P. J. Huber, "Robust estimation of a location parameter," in *Breakthroughs in statistics*. Springer, 1992, pp. 492–518. [3, 14](#)
- [56] F. R. Hampel, "The influence curve and its role in robust estimation," *Journal of the american statistical association*, vol. 69, no. 346, pp. 383–393, 1974. [3](#)
- [57] D. Nogneng and M. Ovsjanikov, "Informative descriptor preservation via commutativity for shape matching," in *Computer Graphics Forum*, vol. 36, no. 2, 2017, pp. 259–267. [4](#)
- [58] Q. Ma, J. Yang, A. Ranjan, S. Pujades, G. Pons-Moll, S. Tang, and M. J. Black, "Learning to Dress 3D People in Generative Clothing," in *Proc. IEEE Conf. CVPR*, 2020, pp. 6469–6478. [6](#)
- [59] G. Pons-Moll, S. Pujades, S. Hu, and M. Black, "Clothcap: Seamless 4d clothing capture and retargeting," *ACM TOG*, vol. 36, no. 4, pp. 1–15, 2017. [6](#)
- [60] Y. Li, H. Takehara, T. Taketomi, B. Zheng, and M. Nießner, "4dcomplete: Non-rigid motion estimation beyond the observable surface," in *Proc. IEEE Int. Conf. Computer Vision*, 2021, pp. 12706–12716. [6](#)
- [61] A. Bozic, M. Zollhöfer, C. Theobalt, and M. Nießner, "Deepdeform: Learning non-rigid rgb-d reconstruction with semi-supervised data," in *Proc. IEEE Conf. CVPR*, 2020, pp. 7000–7010. [6](#)
- [62] F. Xiang, Y. Qin, K. Mo, Y. Xia, H. Zhu, F. Liu, M. Liu, H. Jiang, Y. Yuan, H. Wang, L. Yi, A. X. Chang, L. J. Guibas, and H. Su, "SAPIEN: A simulated part-based interactive environment," in *Proc. IEEE Conf. CVPR*, 2020, pp. 11097–11107. [6](#)
- [63] A. Jacobson, Z. Deng, L. Kavan, and J. Lewis, "Skinning: Real-time shape deformation," in *ACM SIGGRAPH 2014 Courses*, 2014. [6](#)
- [64] X. Liu, C. R. Qi, and L. J. Guibas, "Flownet3d: Learning scene flow in 3d point clouds," in *Proc. IEEE Conf. CVPR*, 2019. [6, 9](#)
- [65] L. G. S. Giraldo, E. Hasanbelliu, M. Rao, and J. C. Principe, "Group-wise point-set registration based on rényi's second order entropy," in *Proc. IEEE Conf. CVPR*, 2017, pp. 2454–2462. [6, 7, 8, 9](#)
- [66] D. S. Hayden, J. Pacheco, and J. W. Fisher, "Nonparametric object and parts modeling with lie group dynamics," in *Proc. IEEE Conf. CVPR*, 2020, pp. 7424–7433. [6, 7](#)
- [67] T. Groueix, M. Fisher, V. G. Kim, B. C. Russell, and M. Aubry, "3d-coded: 3d correspondences by deep deformation," in *European Conference on Computer Vision*, 2018, pp. 230–246. [6, 7](#)
- [68] S. Wang, A. Geiger, and S. Tang, "Locally aware piecewise transformation fields for 3d human mesh registration," in *Proc. IEEE Conf. CVPR*, 2021, pp. 7639–7648. [6, 7](#)
- [69] W. Feng, J. Zhang, H. Cai, H. Xu, J. Hou, and H. Bao, "Recurrent multi-view alignment network for unsupervised surface registration," in *Proc. IEEE Conf. CVPR*, 2021, pp. 10297–10307. [6, 7](#)
- [70] I. Loshchilov and F. Hutter, "Decoupled weight decay regularization," *arXiv preprint arXiv:1711.05101*, 2017. [6](#)
- [71] D. Ulyanov, A. Vedaldi, and V. Lempitsky, "Instance normalization: The missing ingredient for fast stylization," *arXiv preprint arXiv:1607.08022*, 2016. [6](#)
- [72] N. Mayer, E. Ilg, P. Hausser, P. Fischer, D. Cremers, A. Dosovitskiy, and T. Brox, "A large dataset to train convolutional networks for disparity, optical flow, and scene flow estimation," in *Proc. IEEE Conf. CVPR*, 2016, pp. 4040–4048. [9](#)
- [73] C. Choy, W. Dong, and V. Koltun, "Deep global registration," in *Proc. IEEE Conf. CVPR*, 2020, pp. 2514–2523. [9](#)
- [74] Y. Aflalo, H. Brezis, and R. Kimmel, "On the optimality of shape and data representation in the spectral domain," *SIAM Journal on Imaging Sciences*, vol. 8, no. 2, pp. 1141–1160, 2015. [10](#)
- [75] J. Townsend, N. Koep, and S. Weichwald, "Pymanopt: A python toolbox for optimization on manifolds using automatic differentiation," *Journal of Machine Learning Research*, vol. 17, no. 137, pp. 1–5, 2016. [11](#)



Jiahui Huang received his B.S. degree in computer science and technology from Tsinghua University in 2018. He is currently a Ph.D. candidate at the Department of Computer Science and Technology, Tsinghua University. His research interests include computer vision, robotics and computer graphics. His personal webpage is at <https://cg.cs.tsinghua.edu.cn/people/~huangjh/>.



Tolga Birdal is a postdoctoral researcher at the Geometric Computing Group of Stanford University. He has defended his masters and Ph.D. theses at the Computer Vision Group, CAMP Chair, TU Munich. He was also a Doktorand at Siemens AG. His current foci of interest involve geometric machine learning and 3D computer vision. More theoretical work is aimed at investigating the limits in geometric computing, non-Euclidean inference and principles of deep learning. His personal webpage is at <https://www.tbirdal.me>.



Zan Gojcic is currently a research scientist at the NVIDIA AI Lab, which he joined in 2021. He has received his PhD degree from ETH Zurich in 2021, under the supervision of Andreas Wieser. His research interests revolve around 3D computer vision, domain adaptation, and reducing the supervision. His personal webpage is located at <https://zgojcic.github.io/>



Leonidas J. Guibas received his Ph.D. degree from Stanford University in 1976, under the supervision of Donald Knuth. His main subsequent employers were Xerox PARC, MIT, and DEC/SRC. Since 1984, he has been at Stanford University, where he is a professor of computer science. His research interests include computational geometry, geometric modeling, computer graphics, computer vision, sensor networks, robotics, and discrete algorithms. He is a senior member of the IEEE and the IEEE Computer Society.



Shi-Min Hu is currently a professor in Computer Science at Tsinghua University. He received a Ph.D. degree from Zhejiang University in 1996. His research interests include geometry processing, image & video processing, rendering, computer animation and CAD. He has published more than 100 papers in journals and refereed conferences. He is Editor-in-Chief of Computational Visual Media, and on the editorial boards of several journals, including Computer Aided Design and Computer & Graphics.

APPENDIX A

SELF-SUPERVISED FLOW LOSS

In this section we detail the self-supervised flow loss used to train our networks, including the following three terms:

- **Chamfer Loss** encourages \mathbf{X}_k to move as close as possible to \mathbf{X}_l :

$$\mathcal{L}_{\text{chamfer}} := \sum_{\mathbf{x}_k^w \in \mathbf{X}_k^w} \min_{\mathbf{x}_l \in \mathbf{X}_l} \|\mathbf{x}_k^w - \mathbf{x}_l\|_2^2 + \quad (18)$$

$$\sum_{\mathbf{x}_l \in \mathbf{X}_l} \min_{\mathbf{x}_k^w \in \mathbf{X}_k^w} \|\mathbf{x}_k^w - \mathbf{x}_l\|_2^2, \quad (19)$$

where $\mathbf{X}_k^w := \mathbf{X}_k + \mathbf{F}_{kl}$ and the elements \mathbf{x} in \mathbf{X} refer to the points in the point set.

- **Smoothness Loss** encourages the local smoothness of the predicted scene flow for nearby points:

$$\mathcal{L}_{\text{smooth}} := \sum_{\mathbf{x}_i \in \mathbf{X}_k} \frac{1}{|N(\mathbf{x}_i)|} \sum_{\mathbf{x}_j \in N(\mathbf{x}_i)} \|\mathbf{F}_{k,i} - \mathbf{F}_{k,j}\|_2^2, \quad (20)$$

where $(\cdot)_i$ and $(\cdot)_j$ are the point indices and $N(\mathbf{x})$ is the set of k nearest neighbours of \mathbf{x} .

- **Laplacian Loss** enforces the geometric structure depicted by the laplacian coordinate vector is preserved after warping, giving:

$$\mathcal{L}_{\text{lap}} := \sum_{\mathbf{x}_k^w \in \mathbf{X}_k^w} \|\Delta(\mathbf{x}_k^w) - \Delta(\mathbf{x}_l^{\text{inter}})\|_2^2, \quad (21)$$

where $\mathbf{x}_l^{\text{inter}}$ is the interpolated position of \mathbf{x}_k^w on \mathbf{X}_l and the laplace operator is defined as:

$$\Delta(\mathbf{x}_i) := \frac{1}{|N(\mathbf{x}_i)|} \sum_{\mathbf{x}_j \in N(\mathbf{x}_i)} (\mathbf{x}_j - \mathbf{x}_i). \quad (22)$$

For more details please refer to [23]. The only difference between the loss we used and theirs is that we remove the multi-scale supervision on each hierarchy.

APPENDIX B

DETAILS OF THE IRLS SOLVER

The solution to the robust argmin problem is used in both the end-to-end network training (Eq (2)) and the synchronization module (Eq (16)). Hence the computation must be fast and differentiable (*i.e.* $\frac{\partial E_{kl}}{\partial \mathbf{C}_{kl}}$ for back propagation). We use the IRLS algorithm shown in Alg. 1 for the forward pass and the backward pass is achieved by auto-differentiation via unrolling the iterations. The optional input of $\mathbf{C}_{kl}^{[0]}$ is provided as the result from the last iteration (or simply \mathbf{C}_{kl}^0 at the beginning of the optimization) while solving the synchronization problem.

During the weight computation of Λ_{kl} , we define $\omega(\cdot)$ as the influence function of the Huber robust kernel [55], formulated as:

$$\omega(r) := \begin{cases} 1 & \text{if } |r| < \kappa \\ \kappa/|r| & \text{if } |r| \geq \kappa \end{cases}, \quad (23)$$

where the scale factor κ is empirically chosen as 0.05. With such a scale, not only the robustness is maintained but the resulting energy landscape also has few local minima, hence making the convergence reasonably fast within a few iterations. For efficiency considerations, we let $T = 2$ for solving Eq (2) and $T = 1$ for solving one iteration of Eq (16). Note that although we iterate only once for the synchronization, Alg. 1 still needs to be run multiple times

Algorithm 1: Solving the argmin problem with IRLS.

```

1 Input: Aligned bases  $\Phi_k^{kl}, \Phi_l^{kl}$  and optional initial  $\mathbf{C}_{kl}^{[0]}$ .
2 Output: Optimal  $\mathbf{C}_{kl}$ .
3 for  $t \leftarrow 1$  to  $T$  do
4   if  $t = 1$  and  $\mathbf{C}_{kl}^{[0]}$  not exists then
5      $\Lambda_{kl} \leftarrow \mathbf{I}_{I_{kl}}$ .
6   else
7      $r_i \leftarrow \|\Phi_{l,i}^{(kl)} - \Phi_{k,i}^{(kl)} \mathbf{C}_{kl}^{[t-1]}\|, i \in [1, I_{kl}]$ ,
8      $\Lambda_{kl} \leftarrow \text{diag}(\omega(r_1), \dots, \omega(r_{I_{kl}}))$ .
9      $\mathbf{A}_{kl} \leftarrow \Lambda_{kl} \Phi_k^{(kl)}, \mathbf{B}_{kl} \leftarrow \Lambda_{kl} \Phi_l^{(kl)}$ ,
10    Set  $\mathbf{C}_{kl}^{[t]} \leftarrow \mathbf{A}_{kl}^+ \mathbf{B}_{kl}$  or with Eq (17) during
      synchronization (§ 5).
11  $\mathbf{C}_{kl} \leftarrow \mathbf{C}_{kl}^{[T]}$ .
```

during the alternating optimization scheme of $\{\mathbf{H}_k\}$ and $\{\mathbf{C}_{kl}\}$.

APPENDIX C

SOLVING THE RAYLEIGH PROBLEM

As proved by [7], the solution to the problem in the form of Eq (16) after fixing $\{\mathbf{C}_{kl}\}$ is the solution of a generalized Rayleigh problem.

Specifically, we construct the graph connection laplacian matrix $\mathbf{L} \in \mathbb{R}^{KM \times KM}$ as follows:

$$\mathbf{L} = \begin{bmatrix} \mathbf{L}_1 & -\hat{\mathbf{C}}_{12} & \dots & -\hat{\mathbf{C}}_{1K} \\ -\hat{\mathbf{C}}_{21} & \mathbf{L}_2 & \dots & -\hat{\mathbf{C}}_{2K} \\ \vdots & \vdots & \ddots & \vdots \\ -\hat{\mathbf{C}}_{K1} & -\hat{\mathbf{C}}_{K2} & \dots & \mathbf{L}_K \end{bmatrix}, \quad (24)$$

where

$$\hat{\mathbf{C}}_{kl} := \mathbf{C}_{kl} + \mathbf{C}_{lk}^\top, \quad (25)$$

$$\mathbf{L}_k := \sum_{(k,l) \in \mathcal{E}} \mathbf{I}_M + \sum_{(l,k) \in \mathcal{E}} \mathbf{C}_{lk}^\top \mathbf{C}_{lk}. \quad (26)$$

Then the spectral solution $\mathbf{H} \in \mathbb{R}^{KM \times V}$ is given by the V eigenvectors of \mathbf{L} corresponding to the smallest V eigenvalues.